Nature Communications

https://doi.org/10.1038/s41467-026-70155-2

Article in Press

Single-engineered-residue solvation perturbations regulate global protein architecture and function

Received: 7 August 2025

Accepted: 20 February 2026

Cite this article as: Liu, Y., Zhai, J., Cao, S. *et al.* Single-engineered-residue solvation perturbations regulate global protein architecture and function. *Nat Commun* (2026). https://doi.org/10.1038/s41467-026-70155-2

Yingya Liu, Jihang Zhai, Shanshan Cao, Huiying Guo, Hengwei Zhang, Bo Song, Jiajia Guo, Dong Men, Xiao He & Di Li

Single-Engineered-Residue Solvation Perturbations Regulate Global Protein Architecture and Function

Yingya Liu[1,#], Jihang Zhai[1,#], Shanshan Cao[2], Huiying Guo[3], Hengwei Zhang[1], Bo Song[4], Jiajia Guo[3], Dong Men[2,*], Xiao He[1,5,6,7,*], Di Li[1,*]

1 School of Chemistry and Molecular Engineering, East China Normal University, Shanghai, 200241, China

2 Guangzhou National Laboratory, Guangzhou, 510005, PR China

3 Shenzhen Institutes of Advanced Technology, Chinese Academy of Sciences, Shenzhen, 518055, China

4 School of Optical‐Electrical Computer Engineering, Shanghai Key Lab of Modern Optical Systems, University of Shanghai for Science and Technology, Shanghai, 200093, China

5 Shanghai Engineering Research Center of Molecular Therapeutics and New Drug Development, Shanghai Frontiers Science Center of Molecule Intelligent Syntheses, East China Normal University, Shanghai 200062, China

6 Chongqing Key Laboratory of Precision Optics, Chongqing Institute of East China Normal University, Chongqing 401120, China

7 New York University–East China Normal University Center for Computational Chemistry, New York University Shanghai, Shanghai, 200062, China

[*]Corresponding author:

dli@chem.ecnu.edu.cn (D.L.)

xiaohe@phy.ecnu.edu.cn (X.H.)

men_dong@gzlab.ac.cn (D.M.)

Abstract

Protein-water interactions fundamentally shape the structure, stability, dynamics, and functionality of proteins. However, the heterogeneous nature of the protein-water interface and the disparity in their dynamic interplay make it challenging to understand how local water perturbations influence protein structural dynamics over space and time. In this study, we introduce a photochromic molecule, spiropyran, to modify a specific residue of proteins, thereby achieving a reversible, residue-specific, and amplified perturbation on the hydrophobicity of protein surfaces. With the aid of controlled, amplified hydrophobic perturbations, we reveal that even residue-level changes in hydrophobicity induce significant global alterations in protein hydration patterns. These hydration shifts propagate in an amino acid sequence-dependent manner, initiating dramatic influences overall protein architecture and catalytic performance. Our findings establish that interfacial water networks not only capture the surface physicochemical patterns of proteins but also mediate the propagation of local perturbations into broader structural and functional fluctuations. By shifting the paradigm from "structure-function" to "structure-hydration-function", our work provides innovative perspectives into understanding protein architecture and guiding future drug design strategies.

Introduction

Water serves as an active matrix within biological systems, providing a dynamic hydrogen bond network (HBN) that supports protein hydration[1-3]. This hydration water shell bridges the gap between the protein surface and bulk water[4-6], therefore, it is closely implicated in protein folding and plays a critical role in their functions through molecular-level water-protein interactions[7-9]. For instance, protein hydration water can act as a lubricant, aiding the rearrangement of hydrogen bonds during protein conformational change, which facilitates the essential flexibility for protein folding[10]. Moreover, the cooperative effects of hydrophobic solvation and protein-protein interactions constitute key thermodynamic drivers for the formation of liquid-liquid phase separation and subsequent fibrils[3]. Consequently, fine-tuning hydration water presents significant potential for advancements in protein structural engineering and drug design.

The influence of local water perturbations on global protein structures is not yet well understood, partly due to the heterogeneous distribution of charge and hydrophobicity on protein surfaces[11-13]. Polar protein residues stabilize hydrogen-bond-ordered networks, while hydrophobic patches template stratified hydration layers with restricted rotational diffusion but enhanced lateral mobility[14-16]. These spatially segregated nanoscale patches, with distinct hydrogen bond lifetimes, interfacial viscosities, water dynamics, and proton-exchange rates, complicate the task of understanding how water networks span and reshape protein dynamics.

The issue of whether hydrophobic perturbations at individual residues can trigger long-range restructuring of the water layer and regulate the global protein structure remains a topic of contention. NMR and neutron scattering experiments[17], as well as simulation studies, collectively suggest that localized mutations primarily affect the first-shell water (3-5 Å). These perturbations may potentially extend to 2-3 adjacent layers (10-15 Å) via HBNs. Nevertheless, recent evidence from femtosecond time-resolved fluorescence Stokes shift and anisotropy measurements indicated that water perturbations stemming from isolated mutations can exert global effects on solvation, which drives coupled protein side-chain motion[5]. Based on these findings, water perturbations from local residues are hypothesized to induce global conformational reconfiguration, but have

not yet been fully verified. Such discrepancies may arise from small variations in hydrophobicity among amino acids (Kyte-Doolittle scale, -4.5 to 4.5)[18], which obfuscate changes in solvation and present challenges for analysis.

In this study, we address the challenges of hydrophobicity changes at the single-residue level by engineering a specific protein residue with a photochromic molecule, spiropyran (Fig. 1a)[19]. The light-triggered transition between merocyanine (MC) and spiropyran (SP) isoforms results in a marked polarity shift that enhances the hydrophobicity disturbances at the modified residue. Both molecular dynamics (MD) simulations and terahertz (THz) spectroscopy results suggest that alterations in single-residue hydrophobicity not only disrupt local water configurations but also initiate a cascading reorganization of the entire hydration shell. This restructuring of the hydration shell progresses along amino acids in a sequence-dependent manner, triggering a cascading effect that influences global protein architecture and catalytic activities. Our research introduces a predictive "structure-hydration-function" framework that delineates the interplay between protein structure and hydration dynamics, which together determine functional outcomes. These insights lay the groundwork for the strategic design of protein engineering methodologies, presenting an avenue for fine-tuning biomolecular functionality.

Results

Residue-specific Engineering Alkaline Phosphatase (ALP) with Photochromic Molecule

Alkaline phosphatase (ALP, EC: 3.1.3.1) was chosen as a model protein to investigate the impact of local hydrophobicity due to its photostability under 450 nm illumination (Supplementary Figure 1-2). Loop regions, which are crucial for the structural integrity and flexibility of proteins[20,21], are significantly affected by their interactions with water. Using the crystal structure of ALP (PDB 1ED9 [http://doi.org/10.2210/pdb1ED9/pdb]) as a guide[22], specific residues in the loop region, located at varying distances from the catalytic site, were replaced with the unnatural amino acid p-azido-L-phenylalanine (pAzF). The selected sites were H372/872 (~5 Å from the catalytic site), V99/599 (~10 Å), E406/906 (~15 Å), and K185/685 (~25 Å) (Supplementary Figure 3-5)[23]. After comprehensive evaluations of catalytic activity and photo-stability, the E406/906M

mutants (ALP-E15) were chosen for further studies (Supplementary Figure 6-7). To facilitate light-induced reversible and amplified perturbations in hydrophobicity, a dibenzocyclooctyne (DBCO)-functionalized SP (DBCO-SP) molecule (Supplementary Figure 8-10) with reversible photoisomerization (Supplementary Figure 11) and remarkable less hydrophobic-to-more hydrophobic transformation (Fig. 1b) was conjugated to the ALP-E15 through a click reaction (Fig. 1c). The successful conjugation of DBCO-SP to ALP was verified by mass spectra (Fig. 1d) and UV/vis spectra (Fig. 1e). Further quantitative analysis of the solvent-accessible surface area (SASA) indicated that the modified MC/SP accounts for ~4% of the total accessible protein surface (Supplementary Figure 12).

We then investigated the photoisomerization-induced changes of microenvironments on the engineered protein surface by measuring the fluorescence lifetime of MC. As a sensitive reporter for polarity (Supplementary Figure 13), MC exhibits site-dependent fluorescence lifetimes upon conjugating to different sites of ALP, indicating variations in local polarity microenvironment (Supplementary Figure 14-15). The fluorescence lifetimes of ALP-MC and its revertant state (RMC, regenerated by photoisomerization from SP to MC) were recorded by time-correlated single photon counting (TCSPC)[24] (Fig. 1f). Statistical differences in fluorescence lifetime were observed between ALP-MC and ALP-RMC (Fig. 1g). In contrast, negligible variations occurred between free MC and RMC (Fig. 1g, Supplementary Figure 16), indicating that MC-SP isomerization specifically triggers rearrangements of the hydration shell that possibly leads to changes of protein conformation[25].

Rearrangement of Hydrogen Bond Network and Global Protein Hydration

With the capability to enhance the hydrophobicity of a specific protein residue, we probed the photoisomerization-induced rearrangement of HBN within the hydration shell. We conducted MD simulations to investigate the perturbation of local hydrophobicity on the protein-water interface. The simulations were performed on a fully hydrated ALP based on a known structure (PDB ID: 1ED9 [http://doi.org/10.2210/pdb1ED9/pdb]) with MC and SP molecules modified at the mutation sites[26].

We first evaluated the radial distribution function (RDF, (g(r)) of water between water and the modified residue, catalytic site, or the global ALP surface, in response to photoisomerization using the trajectories from the stable phase of each group (Figs. 2a-c and Supplementary Figure 17). At the modified residue, the hydrophilic MC shows a prominent g(r) peak in the 0-4 Å range (first hydration shell), presumably due to a denser, direct HBs between water and the polar groups of the MC probe (Fig. 2d and Supplementary Figure 18). In contrast, SP expels the first shell of water, creating a sub-nanoscale hydrophobic cavity. This leads to a gradual rise of the g(r) peak in the 4-8 Å range. Furthermore, the more mobile outer hydration layer shows higher sensitivity to distal perturbations, resulting in a concerted amplification of HBN reorganization[27]. Consequently, after photoisomerization to SP, the RDF of water around the distant catalytic site (15 Å from the modified site) also exhibits elevated g(r) peaks in the 3-8 Å range. While within 0-4 Å near the catalytic site, the g(r) peak is diminished in the ALP-SP group, which can be ascribed to a disturbance in dipole orientation coupled with a reduction in dielectric shielding[28]. For the global protein, the RDF across the entire ALP surface reveals only a minor decrease in the 3-8 Å range, suggesting that the averaging effect masks local depletion.

To define the spatial range of residue hydrophobicity effects on global water dynamics, we computed lifetime (τ_{HB}) of water-water (w-w) hydrogen bonds within successive hydration layers (1^{st}: < 4 Å, 2^{nd}: 4-6 Å, 3^{rd}: 6-10 Å) around the modified residue[29,30], distal catalytic site, and global ALP surface, respectively (Figs. 2e-g, Supplementary Figure 19). In the 1^{st} and 2^{nd} hydration shells, ALP-SP presented longer τ_{HB} than ALP-MC in all these groups. This might be caused by the expansion of hydrophobic SP interfaces via ordered hydration cages that stabilize τ_{HB}. In contrast, the competing hydrogen bonding between MC and water destabilizes the w-w HB, thereby shortening its lifetime (Fig. 2d). This effect decays over successive hydration layers in a distance-dependent way until reaching bulk water values after three layers. Besides, the most remarkable elongation in HB lifetime was also observed at the catalytic site for both SP and MC groups, which may be ascribed to the disordered dipole alignment in its electrically organized water network[31]. Therefore, we concluded that changes in the hydrophobicity of single residues can laterally

propagate across the protein surface to remote sites, causing global hydration changes (Fig. 2h).

After confirming the stable w-w HB in the 1st hydration layer and the increased mobility of outer hydration layers upon photoisomerization to ALP-SP, we then calculated the water density fluctuations (WDFs) across protein surfaces to investigate the effect on distal residues. WDFs were defined as the probability of finding N water molecules in a 3.5 Å spherical probe volume centered on groups of each hydrophilic/hydrophobic residue (P(%))[32]. Accordingly, its function with the normalized water number fluctuation $[\langle N^2\rangle - \langle N\rangle^2]/\langle N\rangle$ (F_N) acts as an indicator of water exchange dynamics at the residue-water interface. As illustrated in Fig. 2i and Supplementary Figure 20, both ALP-MC and ALP-SP have a bimodal F_N distribution, corresponding to hydrophilic (small F_N) and hydrophobic (large F_N) populations. Notably, in ALP-SP, both peaks shift toward small F_N values with higher P(%), indicating that enhanced local hydrophobicity leads to suppressed global water mobility. Paradoxically, this decreased global water mobility is likely due to the reorganization of water mediated by protein surface topology.

We then quantified the number of hydrogen-bonded (H-bonded) waters ($N_{\text{H-bonded water}}$) per solvent-accessible residue to explore the residue-specific physicochemical properties on the propagation induced by local perturbations. The difference value in H-bonded waters ($\Delta N_{\text{H-bonded water}}$) for each residue, calculated by subtracting ALP-MC from ALP-SP (ALP-SP – ALP-MC), was then mapped onto the corresponding residues to provide a direct perspective on global hydration alterations (Fig. 2j). Highly perturbed patches (increased $N_{\text{H-bonded water,}}$ red) and lowly perturbed patches (decreased $N_{\text{H-bonded water,}}$ blue) discretely coexist across the protein surface, indicating that the hydration changes are heterogeneous and site-specific.

We next divided amino acids into four groups according to their physicochemical properties, including negatively charged (Asp, Glu), positively charged (Lys, Arg, His), polar uncharged residues (Ser, Thr, Asn, Gln, Cys, Tyr), and nonpolar residues (Ala, Val, Leu, Ile, Met, Pro, Phe, Trp, Gly). Then the $\Delta N_{\text{H-bonded water}}$ per residue category (calculated as ALP-SP – ALP-MC) was subjected to normal distribution analysis (Fig. 2k-n, Supplementary Figure 21-22). Here, the mean $\Delta N_{\text{H-bonded water}}$ (μ) represents the average net change per residue, whereas the standard deviation

(σ) quantifies the degree of spatial heterogeneity in hydration dynamics in responses to photoisomerization. Notably, all types of residues, especially positively charged residues, showed positive changes in $N_{\text{H-bonded water}}$ ($\mu>0$), indicating a global net increase in $N_{\text{H-bonded water}}$ upon photoisomerization to ALP-SP. The increase implies that changes in local hydrophobicity disrupt long-range water networks, freeing water molecules to enhance local entropy and drive global hydration restructuring. Moreover, negatively charged groups exhibited the greatest $\Delta N_{\text{H-bonded water}}$ variability and the broadest frequency distribution ($\sigma = 0.989$), indicating the highest sensitivity to local perturbations. Positively charged and polar groups showed similar medium fluctuations and distribution widths. Conversely, nonpolar groups demonstrated the least fluctuations and the narrowest distribution with the highest frequency in ΔN = -0.5 to 0.5. This suggests that the propagation pathways of hydrophobicity perturbations are influenced by the electrostatic/polarity characteristics of different amino acids via HBN tuning[33], in the sequence of negatively charged > positively charged ≈ polar (neutral) > nonpolar[34]. We concluded that the local photoisomerization-induced HBN disruption at the modified residue triggers a long-range reorganization of water across the protein surface, with propagation pathways modulated by the surface chemical microenvironment.

We next employed in situ Attenuated Total Reflection Terahertz **(**ATR-THz) spectroscopy to probe dynamic variations in protein hydration. The THz regime is exquisitely sensitive to perturbations in collective HBNs[35], enabling direct detection of HB stretching (ν_{HB}, 150-200 cm^{-1}) and librational modes (ν_{Lib}, 450-600 cm^{-1}) of hydration water[36,37]. Measurements were performed on protein film samples prepared at precisely controlled hydration levels[38]. Protein films were formed by drying solutions onto an IR-transparent diamond under gentle vacuum, followed by application of Tris-NaCl buffer to achieve target hydration levels (see SI for details). Significantly, stable intensity at 1550 cm^{-1} ($\Delta R_{\text{hy}} < 0.02$; water-content internal standard) confirms constant water content after photoisomerization (Eq. S1-S2, Supplementary Figure 23).

To minimize bulk water interference and elucidate the reorganization of hydration water, THz spectra were measured across distinct hydration levels: low hydration state (~ 0.2 g H_2O/g protein),

corresponding to a discontinuous sub-monolayer hydration regime on the protein surface; moderate hydration state (~ 0.7 g H_2O/g protein), which fully saturates the first hydration shell and partially populates the second shell; high hydration state (~ 1.2 g H_2O/g protein), approaching completion of the first three hydration shells[9,39] (Fig. 3a-c and Supplementary figure 24-25, Supplementary Table S1). The single-beam ATR spectra of ALP-MC and ALP-SP at different hydration levels were converted to absorbance spectra by penetration depth correction[40] (Fig. 3d).

We then examined how hydration level governs the THz frequency shifts triggered by the ALP-MC to ALP-SP photoisomerization (Fig. 3e, f). In the fully hydrated group, the HB stretching band (ν_{HB}) was centered at ~ 130 cm^{-1} for both ALP-MC and ALP-SP. In comparison, the librational band (ν_{Lib}) shifted from 539 cm^{-1} (ALP-MC) to 545 cm^{-1} (ALP-SP). This small change is likely attributed to the buffered local disturbances by the HBN of bulk water. However, at reduced hydration level (~ 0.7 and 0.2 g/g), both modes exhibit larger blue-shifts after photoisomerization to ALP-SP with ν_{Lib} shifted from 586 to 612 cm^{-1} (~ 0.7 g/g) and 584 to 614 cm^{-1} (~ 0.2 g/g), while ν_{HB} shifted from 170 to 195 cm^{-1} (~ 0.7 g/g) and 165 to 196 cm^{-1} (~ 0.2 g/g). These changes indicate the formation of a cooperatively rigidified HBN in the protein hydration layer that enhances the orientational order of water molecules[41,42]. Consistently, ATR-THz experiments with reversible ALP-RMC photo-switching reveal that the hydration layer is unable to fully revert to its initial state (Supplementary Figure 26). This indicates that a localized perturbation can induce a global and irreversible transition in protein hydration. Moreover, control experiments using pure water and native ALP ruled out possible contributions from light-induced heating effect on structural changes in the solvent or protein (Supplementary Figure 27-28). Consequently, the THz results demonstrated that a single-residue hydrophobicity change can induce HBN reorganization across global hydration. Moreover, this conversion is amplified under reduced hydration levels, hinting that the hydration layer may act as a critical regulator of biological interfaces.

To delineate the thermodynamic basis of light-induced hydration rearrangements between ALP-MC and ALP-SP, we used THz calorimetry to correlate spectral changes with entropy (ΔS)

and enthalpy (ΔH). Absorption coefficients ($\alpha(\nu)$) and photoisomerization-induced differential spectra ($\Delta\alpha(\nu)_{SP\text{-}MC}$, ALP-SP minus ALP-MC) were calculated to isolate hydration-specific alterations (Eqs. 1-3, Supplementary Figure 29). The $\Delta\alpha(\nu)_{SP\text{-}MC}$ was deconvolved into the hydrophobic "wrap" region (150-200 cm^{-1}, entropy-linked) and hydrophilic "bound" region (450-600 cm^{-1}, enthalpy-linked) (Supplementary Figure 30).

Spectral analysis of $\Delta\alpha(\nu)_{SP\text{-}MC}$ spectra at different hydration levels revealed a negative $\Delta\alpha_{wrap}$ amplitude ($\Delta\alpha_{wrap} < 0$), signifying a positive entropy change ($\Delta S > 0$, Eq. 4 and S3, Supplementary Table S2) due to the release of loosely wrap-water from hydrophobic patches (Fig. 3g). Concurrently, a positive slope in the bound region ($\Delta\alpha_{bound}/\Delta\nu > 0$) indicated a negative enthalpy change ($\Delta H < 0$, Eq. 5), reflecting enhanced rigid H-bond networks with hydrophilic residues. Consequently, the THz results demonstrated that a single-residue hydrophobicity change can induce HBN reorganization across global hydration by converting water from a loosely associated "wrap-water" state to a tightly bound, ordered configuration, thereby forming a rigid hydration layer. Furthermore, the observed entropy-enthalpy compensation minimizes the system's free energy, yielding a net favorable hydration contribution ($\Delta G^{hydration} < 0$, Eq. 6) that acts as the thermodynamic driver for conformational destabilization.

We then calculated THz spectra of global and residue-local hydration shells via auto-correlation functions of the time derivative of dipole based on MD simulations to distinguish the origin of THz peak shifts[43], whether they arise from global hydration layer reorganization or localized hydrophobic changes by MC/SP photoisomerization. The raw MD-calculated spectra of bulk water without smoothing or signal extraction are provided to maintain statistical precision (Supplementary Figure 31). The employed qSPC/Fw water model exhibits a known force-field limitation that precludes the capture of the 200 cm^{-1} peak[44,45]. Nonetheless, it qualitatively reproduces the librational band above ~300 cm^{-1}, showing agreement with the experimental spectrum of ambient water (Supplementary Figure 32). The known systematic blueshift does not impact the relative trends under discussion.

This allows for comparison of librational mode changes in hydration water after

photoisomerization to ALP-SP. The THz spectral peak shifts are analyzed separately for the hydration layer around the modified-MC site and the global hydration layer of protein but excluded MC-modified sites. After photoisomerization from MC to SP, there is a blue shift of librational modes in both local hydration at the modification site (Fig. 3h) and the global protein hydration layer but excluded MC-modified sites (Fig. 3i). This confirms that the experimentally observed THz peak shifts originate primarily from hydration shell restructuring, rather than from site-specific vibrational amplification.

Global Protein Structural and Functional Changes Induced by the Rearrangement of HBN

We next probed the role of HBN rearrangement in mediating distal protein structural changes. After ensuring the systems were stable (Fig. 4a, Supplementary Figure 33)[46], we scrutinized the differences in structural fluctuation of ALP-SP and ALP-MC through the root mean square fluctuation (RMSF) of protein backbone atoms. As illustrated in Fig. 4b, the difference in RMSF between ALP-MC and ALP-SP (ΔRMSF) indicates that ALP undergoes residue-specific conformational fluctuations. To depict the spatial distribution of these fluctuations, we mapped ΔRMSF values onto their corresponding residues. Notably, compared to ALP-MC, ALP-SP demonstrated enhanced fluctuations in regions containing SP modifications and in adjacent loop regions (Fig. 4c). The superimposition of simulated structures of ALP-MC and ALP-SP further validated these distinct conformational fluctuations and structural alternations (Fig. 4d). Specifically, we observed a rigidification in the secondary structure at residues 902-922 (SP modification site) and 823-835 (catalytic active site). Analysis of secondary structure evolution over the final 20 ns confirmed these differences persist (Supplementary Figure 34-36). The distance matrix (DM) analysis revealed an increased intramolecular distance in ALP-SP (Fig. 4e, f), suggesting reduced cooperativity among residues, which may lead to less compact global structures. Importantly, control simulations of the ALP-N_3 mutant confirmed that the overall protein fold remains unperturbed by covalent modification alone, whereas the light-induced hydrophobic switch selectively enhances local flexibility and remodels the hydration shell (Supplementary Figure 37-38).

To further evaluate the role of specific MC/SP-surface interactions, we conducted MM/GBSA energy decomposition. The results show that interactions near modified MC/SP are mainly electrostatic, with negligible van der Waals contributions. Solvent water strongly screens these electrostatic effects beyond ~5 Å. Despite differing charge distributions, both isoforms exhibit highly similar interaction profiles with surface residues (Supplementary Figure 39). Therefore, the observed changes in flexibility and stability are more likely due to HBN reorganization instead of direct effect of the modification.

To corroborate the MD simulations, small-angle X-ray scattering (SAXS) experiments were conducted to investigate the structural dynamics[47,48]. A close alignment between the MD-calculated and experimental scattering profiles (χ^2 <1.7) substantiates the accuracy of the simulations (Fig. 4g). Guinier analysis revealed an increase in R_g (36.93→38.63 Å; Fig. 4h) and D_{max} (109→122 Å; Fig. 4i) from ALP-MC to ALP-SP ($P < 0.01$), indicating enhanced structural flexibility. The broadening of the Kratky plot peak was also observed in ALP-SP (Fig. 4j), a characteristic of global structural loosening that is not fully reversible upon relaxation back to the MC state (Supplementary Figure 40-41, Supplementary Table S3). Control experiments with unmodified ALP showed negligible changes in SAXS after photoisomerization (Supplementary Figure 42). Upon photoisomerization to ALP-SP, the thermal denaturation melting temperature also declined by 5 ℃, providing further evidence for the less structured state (Supplementary Figure 43). Collectively, the MD simulations, SAXS and melting temperature data suggest that light-induced hydrophobic perturbations at single residues induce not only local structural rigidity but also propagate to more distal regions, thereby augmenting global protein conformational flexibility.

Having confirmed that the hydrophobic changes of single residues can alter global protein structural dynamics via collective reorganization of HBN, we next investigated the enzymatic changes by interrogating hydrophilic (pNPP) and hydrophobic (4-MUP) substrates (Fig. 5a). For pNPP, after photoisomerization from ALP-MC to ALP-SP, Michaelis constant (K_m) increased ca. 50% and catalytic constant (k_{cat}) dropped ca. 37% (Fig. 5b). The reduced substrate affinity and

catalytic activity suggest that HBN reorganization enhances interfacial water ordering that impedes the delivery of hydrophilic pNPP via solvation-coupled transport[49]. We further employed deuterated reagents in the pNPP assay to verify the influence of hydration on enzymatic activities. As illustrated in Fig. 5c, the reaction rates of both ALP-MC and ALP-SP were markedly suppressed in D_2O, attributable to the stronger deuterium bonding and more ordered HBN structure in D_2O. These require higher enthalpic energy to be disrupted, thereby hindering the access of pNPP to the catalytic pocket[50]. Moreover, the amplified rate difference between ALP-MC and ALP-SP in D_2O further confirmed that the regulation of enzyme function primarily stems from the hydration-layer HBN reorganization, rather than local electric field-induced water orientation. This is supported by the comparable dielectric constants of H_2O and D_2O, which yield consistent electric field effects.

To exclude nonspecific effects from the free photo isomers, we performed a control experiment in which unmodified ALP was mixed with SP. Illumination of this mixture resulted in negligible changes in enzymatic activity. This is in stark contrast to the significant effects observed with covalently conjugated ALP-SP, confirming that functional modulation arises from local perturbations of the hydration shell enabled by site-specific attachment rather than direct interactions with free photoisomers (Supplementary Figure 44).

Furthermore, to exclude potential interference from light-induced hydrophobic aggregation on enzymatic changes, OTG-supplemented experiments were designed. OTG suppressed the possible hydrophobic aggregation but did not reverse activity modulations, confirming that hydration effects primarily regulate enzymatic function (Supplementary Figure 45).

In contrast, the hydrolysis of hydrophobic substrate, 4-MUP, was less influenced by photoisomerization. The K_m and k_{cat} values remained unchanged in both H_2O and D_2O buffer (Fig. 5d-e). This is attributed to the hydrophobic nature of 4-MUP, which allows direct binding to the dehydrated active site, thereby bypassing solvent-mediated hydration processes. Collectively, these findings confirm that the reorganization of HBN can regulate catalytic efficiency through a structure-hydration-function coupling mechanism[51].

To establish physiological generalizability, we introduced single-point mutations at a conserved surface residue (ALP E406/905) using amino acids with varying hydrophobicity (I > F > G > Q > K) (Supplementary Figure 46a). A clear correlation emerged between residue hydrophobicity and activity toward the hydrophilic substrate pNPP (activity: I < F < G < Q), while activity toward the hydrophobic substrate 4-MUP remained largely unchanged (Supplementary Figure 46b-c). The Lys (K) variant, likely modulating hydration via charge effects, was an exception. These results, alongside those from the SP/MC system, confirm that water-mediated allostery constitutes a general and tunable mechanism of protein regulation.

Discussion

By integrating a photochromic spiropyran at a certain residue of protein, which induces an amplified and tunable hydrophobic perturbation, we overcome the inherent noise of natural hydrophobic variations. This strategy enables quantitative dissection of vertical (depth-dependent) and horizontal (laterally propagating) water reorganization. Synergized MD simulations and THz spectroscopy reveal that hydration dynamics can trigger a cascading effect that ultimately drives long-range structural reconfiguration of the protein and remodels catalytic activity, establishing a predictive structure-hydration-function framework.

Our findings reveal a hydration heterogeneity in governing protein dynamics, where interfacial waters not only encode surface physicochemical patterns but also hierarchically transduce local perturbations into functional outcomes, from residue-specific hydrophobicity changes to global structural rearrangements. This redefines the protein regulation beyond classical “structure-function” duality, offering foundational insights for hydration-centric drug design and biomolecular recognition.

Methods

Mutant Alkaline Phosphatase (ALP) Expression and Purification. Alkaline phosphatase (ALP; EC 3.1.3.1) was selected as the model protein. The phoA gene (NCBI: NC_000913.3), encoding a C-terminal 6×His tag, was synthesized (GenScript) and cloned into pET28a (Novagen), yielding pET28a-phoA. To site-specifically incorporate p-azido-L-phenylalanine (pAzF) at defined distances from the catalytic center, amber (TAG) mutations were introduced at residues His872/372 (5 Å), Val599/99 (10 Å), Glu906/406 (15 Å), and Lys685/185 (25 Å) using site-directed mutagenesis kit (Mut Express® II Fast Mutagenesis Kit V2; Novartis). Plasmid and primer sequences are provided in Supplementary Data 1. Each TAG-mutant pET28a-phoA plasmid was co-transformed with pEVOL-pAzF (Addgene, plasmid no. 31186) into *Escherichia coli* BL21(DE3) (Novagen). Cells were cultured in LB medium with 50 μg/mL kanamycin (Sigma-Aldrich) and 34 μg/mL chloramphenicol (Sigma-Aldrich) at 37 °C. At OD_{600} ~0.4, expression was induced with 1 mM IPTG (Sigma-Aldrich), 1 mM pAzF, and 0.2% (w/v) L-arabinose (Sigma-Aldrich), followed by incubation at 25 °C for 16 h. ALP variants were purified sequentially by nickel-affinity chromatography (HisTrap HP column; Cytiva) and anion-exchange chromatography (Q Sepharose™ column, Cytiva). Purity and integrity were assessed by SDS-PAGE, BCA assay, and LC-MS (Thermo Fisher Scientific).

Synthesis of dibenzocyclooctyne (DBCO)-functionalized SP (DBCO-SP). The IM2 (1'-(2-hydroxyethyl)-3', 3'-dimethylspiro [chromene-2, 2'-indoline] -6-sulfonate) was prepared according to previous literature[52]. DBCO-SP was synthesized via DCC/DMAP-mediated esterification of IM2 with DBCO-C6-acid. A 50 mL round-bottom flask containing DBCO-C6-acid (309.8 mg, 929.2 μmol, 1.20 equiv), DCC (319.5 mg, 1.55 mmol, 2.00 equiv), and DMAP (18.9 mg, 154.9 μmol, 0.20 equiv) in anhydrous DCM (20 mL) was purged with N_2. The mixture was stirred at 25 °C for 1 h to activate the carboxylic acid, then IM2 (300 mg, 774.3 μmol, 1.00 equiv) was added. After stirring at 25 °C for 16 h, the crude product was purified by preparative HPLC (C18 column, isocratic elution with 50:50 v/v CH_3CN/0.1% aq. NH_4OH) to afford DBCO-SP as a brown solid (175 mg, 32.2% yield). Structural confirmation was performed by ^1H NMR, (Bruker Avance III 400 MHz), and liquid chromatography-mass spectrometry (LC-MS; Thermo Fisher Scientific). Photoisomerization characterization was carried out using a UV-visible spectrophotometer (Tecan) as described in Supplementary Information.

Preparation of SP-modified ALP. Azide-functionalized mutant alkaline phosphatase (ALP-N_3, 20 μM) in 25 mM Tris-NaCl (pH 7.5) was reacted with DBCO-SP (10 mM in DMSO) at a 10:1 molar ratio (DBCO-SP: ALP-N_3). The mixture was incubated at 25°C for 2 h or 4°C overnight with gentle agitation. Reaction products were purified using a 7 kDa MWCO spin desalting column (1,200 ×g, 2 min) to remove unreacted DBCO-SP and byproducts, followed by concentration via 30 kDa centrifugal filtration (6,000 ×g, 10 min). Mutant ALP and ALP-SP conjugates (1 mg/mL in 25 mM Tris-NaCl, pH 7.5) were buffer-exchanged and purified using a Superdex™ 200 Increase 10/300 GL column (Cytiva) equilibrated with 25 mM Tris-HCl, 100 mM NaCl (pH 7.5). The separation was performed at 25 °C with a flow rate of 0.5 mL/min, and fractions corresponding to monomeric conjugates were collected. Mass analysis was performed on a Q-Exactive Plus mass spectrometer (Thermo Fisher Scientific) coupled to an Acquity UPLC system (Waters).

Deconvoluted masses were determined using BioPharma Finder 5.3 to confirm the conjugation.

Fluorescence lifetime measurement. Measurements were performed at 20°C using a MicroTime 200 system (PicoQuant) with 532-nm pulsed excitation (40 MHz; LDH-P-FA-530B laser). Fluorescence was collected through a 100×/1.45 NA oil immersion objective, filtered via 488/532 nm dichroic mirror and 582/64 nm bandpass filter (Chroma), and detected by single-photon avalanche diode (Excelitas SPCM-AQRH-14-TR). Mutant ALP variants (V10, E15, K25) were diluted to 100 pM in TAE buffer with oxygen scavenging system (2.5 mM protocatechuic acid, 25 nM protocatechuate-3,4-dioxygenase). Samples were deposited on Ni^{2+}-functionalized coverslips for 10 min[53,54]. All measurements were performed in six independent experimental replicates, each prepared from separately diluted samples and measured on independently prepared coverslips. For photoconversion studies, the MC state was obtained following 1 h of dark adaptation, and the RMC state was generated via 450 nm illumination (10 min) followed by 2 h of subsequent dark adaptation. FLIM images were acquired by galvanometric scanning. Individual molecules were manually selected for lifetime extraction. Fluorescence decays were fitted to multi-exponential models using SymPhoTime 64 software.

Hydrated protein film preparation and THz spectroscopy measurements. Hydrated protein films with hydration levels ranging from 0.02 to 0.4 g H_2O/g protein were prepared using a humidity-controlled method (Methods details are available in Supplementary Information). Terahertz (THz) spectra were recorded using a Fourier-transform infrared (FTIR) spectrometer (Vertex 80v; Bruker, Billerica, MA, USA) equipped with a deuterated L-alanine triglycine sulfate (DLaTGS) detector and a single-reflection attenuated total reflection (ATR) unit (diamond crystal, 45° incidence angle) in the sample compartment. The spectral range was set to 50-690 cm^{-1} with a resolution of 2 cm^{-1}. Both the sample compartment and interferometer compartment were evacuated to a pressure of 2-3 mbar prior to measurement to minimize water vapor interference. Each spectrum was acquired as an average of 64 scans. All THz measurements were performed in three independent experimental replicates, each prepared from independently hydrated protein films and measured separately. The diamond ATR crystal was sequentially cleaned with ultrapure water (prepared using a Milli-Q Integral water purification system; MilliporeSigma), 0.5 M NaOH solution (Sigma-Aldrich), ethanol (Sigma-Aldrich) and dried under a stream of nitrogen gas (99.999% purity; Air Liquide) after each measurement.

THz Spectra and Data Analysis. The ATR absorption coefficient (α(ν)) was calculated using the Lambert-Beer law:

$$\alpha(\nu) = -\frac{1}{d_p}\ln\left(\frac{I(\nu)}{I_0(\nu)}\right) \quad (1)$$

$$d_p = \frac{\lambda}{2\pi\sqrt{n_{diamond}^2 \sin(\theta)^2 - n_{simple}^2}} \quad (2)$$

where $I(\nu)$ and $I_0(\nu)$ denote the sample's and reference's frequency-dependent intensities. The theoretical upper limit for the penetration depth (d_p) indicates how far the evanescent wave can penetrate the sample. The refractive index (n_{diamond}) of diamond is 2.38, while that of liquid samples (n_{sample}) is set to 1.5. For simplicity, the refractive index of the sample was assumed to be the average of water at this frequency range. λ is the wavelength of the radiation, θ is the incident

angle (here θ=4/π).

Difference spectra Δα(ν) were determined by subtracting the ALP-MC spectrum from ALP-SP spectrum, as shown in eq.3:

$$\Delta\alpha(\nu) = \alpha(\nu)_{\text{ALP-SP}} - \alpha(\nu)_{\text{ALP-MC}} \quad (3)$$

Connecting Thermodynamics to Spectroscopy. Within the THz-calorimetry framework, the hydration entropy (ΔS) and enthalpy (ΔH) changes upon photoisomerization are deconvolved into hydrophobic (cavity-wrap) and hydrophilic (bound) contributions via linear correlations with their respective spectroscopic fingerprints.The correlations $\Delta S \propto \Delta\alpha_{\text{wrap}}$ and $\Delta H \propto (\Delta\alpha_{\text{bound}}/\Delta\nu)$ were established using pre-calibrated conversion factors:

$$\Delta S^{\text{hydration}} = \Delta S_{\text{cavity}} + \Delta S_{\text{bound}} \approx \Delta S_{\text{cavity}} = \Delta\alpha_{\text{wrap}}\Delta\bar{S}_{\text{wrap}} \quad (4)$$

$$\Delta\bar{S}_{\text{wrap}} = -4.4\ \text{J}\cdot\text{mol}^{-1}\text{K}^{-1}\text{cm}$$

$$\Delta H^{\text{hydration}} = \Delta H_{\text{cavity}} + \Delta H_{\text{bound}} \approx \Delta H_{\text{bound}} = \Delta\alpha_{\text{bound}}/\Delta\nu\Delta\bar{H}_{\text{bound}} \quad (5)$$

$$\Delta\bar{H}_{\text{wrap}} = -320\ \text{kJ}\cdot\text{mol}^{-1}\text{cm}$$

$$\Delta G^{\text{hydration}} = \Delta G_{bound} + \Delta G_{cavity} \approx \Delta H_{bound} - T\Delta S_{cavity} \quad (6)$$

where $\Delta\alpha_{\text{wrap}}$ and $\Delta\alpha_{\text{bound}}/\Delta\nu$ are the spectroscopic amplitudes in the 150-200 cm^{-1} regions and the slope in 450-600 cm^{-1} regions, respectively. $\Delta\bar{S}_{\text{wrap}}$ and $\Delta\bar{H}_{\text{bound}}$ are constant correlation factors that reported based on a large set of solutes.

SAXS Characterization. SAXS experiments were performed on the BL19U2 beamline of Shanghai Synchrotron Radiation Facility (SSRF). Using an X-ray wavelength (λ) of 1.033 Å, scattered intensities were recorded with a Pilatus 1M detector (DECTRIS Ltd). The sample-to-detector distance was set to 2.6 m, yielding a momentum transfer range ($q = 4\pi\sin\theta/\lambda$, where 2θ is the scattering angle) of 0.01-0.4 $Å^{-1}$, corresponding to a spatial resolution of 10-600 Å. Samples (ALP-dark, ALP-vis, ALP-MC, and ALP-SP) were prepared as 1 mg/mL solutions (100 μL) and maintained at 20°C. Each sample was measured in three independent replicates using separately prepared aliquots across multiple beamtime sessions to ensure statistical robustness. For each sample and buffer, 20 frames were recorded to optimize signal-to-noise ratio. Two-dimensional scattering patterns were azimuthally averaged, solid-angle corrected, and normalized to transmitted beam intensity using BioXTAS RAW 1.2.1. Primary SAXS data analysis was performed with the ATSAS 3.0.3 suite, including Guinier analysis, pair distance distribution (P(r)) calculations, and Kratky plot assessment. Theoretical scattering profiles were generated from crystal structures (ALP-dark, ALP-vis) and MD-simulated structural ensembles (ALP-MC/ALP-SP). For MD-derived models, representative conformations were selected by structural clustering of trajectories, followed by energy minimization of each cluster centroid. Theoretical SAXS curves were computed and fitted against experimental data, with agreement quantified by the goodness-of-fit (χ^2). Detailed acquisition and analysis parameters are summarized in Supplementary Table 4.

MD Model building. The initial model was derived from the RCSB PDB database with the PDB

ID of 1ED9 [http://doi.org/10.2210/pdb1ED9/pdb][22]. Referring to the research of Hou et al. on the catalytic reaction mechanism of ALP phosphorylase[26], the Ser102 residue was modified to a deprotonated state. Meanwhile, the protein was protonated under the condition of pH = 7.5. The covalent modifications at the MC and SP mutation sites were accomplished by the CovCom program. The protein system was characterized by the FF14SB force field[55]. Regarding all non-standard residues, such as those with covalent modifications and the deprotonated SER, the Restrained Electrostatic Potential (RESP) charges were calculated via Gaussian[56]. Subsequently, the parameters were fitted using the GAFF2 force field[57]. For the Zn^{2+} and Mg^{2+} ions located at the active site, the $LJ_{12\text{-}6\text{-}4}$ non-bonding force field parameters, which were meticulously fine-tuned by Li et al.[58,59], were adopted.

The solvation of the MC and SP models was carried out using the LEaP module. A periodic cubic box was constructed, and it was ensured that the distance between the box edges and the protein atoms was greater than 15 Å. The system was then solvated using the flexible fixed-charge qSPC/Fw water model[45]. Meanwhile, Na^+ and Cl^- ions were added to the box to ensure the electrical neutrality of the system. To ensure statistical robustness, four independent molecular dynamics simulations were performed, each initiated from a distinct initial configuration. Details of the initial simulation setup are provided in Supplementary Table S5.

MD simulation details. For both the MC and SP models, four-step minimization was performed using PMEMD[60] to eliminate atomic clashes. In the first minimization step, the protein and the metal ions at the active site were fixed, while the water molecules and counter ions were optimized. In the second minimization step, the protein was fixed, and the water molecules, counter ions, and the metal ions at the active site were optimized. For the third and fourth minimization steps, no restrictions were imposed. Each of the four-step minimizations consisted of 2000 steps of conjugate-gradient optimization, followed by 6000 steps of steepest-descent optimization. Subsequently, the PMEMD.cuda was employed to perform system heating and density relaxation. During the heating stage, a Langevin thermostat was utilized within the NVT ensemble. With a timestep of 1 fs/step, the temperature was gradually increased to 300 K over a period of 100 ps. The density relaxation is also carried out four times, using the NPT ensemble. The time step is set to 1 fs/step, and each relaxation lasts for 50 ps to allow the system density to relax to 1.0 g/cm³. Finally, PMEMD.cuda was used to perform a 500 ns MD (molecular dynamics) simulation for each system under the NVT ensemble, with a timestep of 2 fs/step. Subsequently, for the conformation of each system in the dynamically stable stage, a 50 ps MD simulation with a timestep of 0.5 fs/step was carried out to calculate the hydrogen bond lifetime of the water outside the protein.

CovCom. CovCom mainly relies on BioPython[61] and RDKit[62]. First, it uses BioPython to extract the residue atoms within 25 angstroms around the modification site and convert them into a format recognizable by RDKit. Next, RDKit was employed to splice the modified residues with the modified molecule, and a simple geometric optimization of the modified part is carried out based on the MMFF94 force field[63]. Finally, the atomic coordinates of the modified part are refined by simulated annealing to optimize the binding pose of the new molecule within the cavity formed by surrounding residue atoms within 25 Å. The program code is available at

https://github.com/iawnix/CovCom.

MD simulation analysis. The RMSD (Root Mean Square Deviation) of the protein backbone (C_α, C, N, and O) is used to evaluate the kinetic stability of the two models. The dynamically stable stage (the last 20 ns) was selected for the analysis of RMSF (Root Mean Square Fluctuation), RDF (radial distribution function), and secondary structure. The analysis of RMSF and secondary structure was completed based on CPPTRAJ[60]. According to formula 7, the radial distribution functions of ALP phosphorylase (non-hydrogen atoms), mutation sites (non-hydrogen atoms), and the ions in active sites (Zn^{2+}, Mg^{2+}) with WAT@O in the system are calculated respectively. This process is completed based on MDAnalysis[46].

$$g_{ab}(r)=\frac{\rho_{ab}(r)}{N_b/_V} \tag{7}$$

Hydrogen bond analysis. The last 20 ns of the stable phase of the two systems is selected to count the number of hydrogen bonds between the mutation sites and water. The analysis of the hydrogen bond lifetime between water molecules in different water shell layers is derived from the kinetic sampling of the stable conformation with a time step of 0.5 fs for 50 ps. Following formula 8, the hydrogen bond lifetime (τ) is obtained through single-exponential fitting[29], and this process is completed based on MD analysis.

$$C(t)=\frac{\langle h(0)\cdot h(t)\rangle}{\langle h\rangle} \tag{8}$$

Infrared absorption spectroscopy analysis. For a system in thermodynamic equilibrium, according to the linear response theory[64], the spectrum of the autocorrelation function of the total dipole moment derivative, $\dot{\mu}(t)$, is proportional to the product of the infrared spectral coefficient and the refractive index[44]:

$$\alpha(w)n(w)\propto \int dte^{iwt}\langle\dot{\mu}(0)\dot{\mu}(t)\rangle \tag{9}$$

$$\dot{\mu}(t)=\sum q_i \frac{\partial \vec{r}_{i,t}}{\partial t}=\sum q_i \vec{v}_i \tag{10}$$

Based on Equation (9-10), we calculated the infrared absorption spectra of the 9 Å hydration shell around the mutation site and the 9 Å hydration shell around the protein with the mutation site excluded for the two systems, respectively, to characterize the hydrogen bond network strength of hydration layers in different regions. The trajectories were derived from 50 ps molecular dynamics sampling with a 0.5 fs time step, performed on stable conformations.

The Stability of ALP enzymatic activity against blue light illumination. The enzymatic activity of alkaline phosphatase (ALP) against light illumination was determined using p-nitrophenyl phosphate (pNPP) as a substrate. The hydrolysis products of p-nitrophenol (pNP) were continuously monitored at 405 nm (ε = 18,300 $M^{-1}cm^{-1}$) on a Tecan plate reader. The reaction mixture consisted 50 nM ALP and 1 mM pNPP in assay buffer (25 mM Tris, 100 mM NaCl, pH 7.5). Before reaction, ALP was subjected to blue light illumination (450 nm) for different time intervals. The enzymatic activity of wild-type ALP and site-specific mutants were evaluated under identical conditions. Each measurement was performed in three independent experimental replicates, using separately prepared ALP samples.

Michaelis-Menten Kinetics Analysis. The Michaelis-Menten kinetics of MC-modified ALP were assessed under dark conditions and blue-light illumination using pNPP as a substrate. The reactions were initiated by incubating 50 nM enzyme in a reaction buffer (25 mM Tris, 100 mM NaCl, pH 7.5) with various concentrations pNPP (from 0 to 600 μM). The reaction rates were determined from the linear accumulation of pNP absorbance at 405 nm. The hydrolysis of 4-Methylumbelliferyl phosphate (4-MUP) at 25°C were monitored fluorometrically (λ_{ex} = 360 nm, λ_{em} = 450 nm). The reactions were initiated by incubating 5 nM ALP-MC with various concentrations of 4-MUP (from 0-500 μM). The reaction rates were determined by examining the linear accumulation of 4-methylumbelliferone (4-MU) over a period of 30 minutes, at 1 min intervals. Fluorescence intensities were then converted into 4-MU concentrations through the standard curve. All kinetic measurements were performed in three independent replicates, each initiated from separately prepared reaction mixtures. k_{cat} and K_M values were obtained by fitting the Michaelis-Menten equation.

Quantification and statistical analysis. Data are presented as mean ± standard deviation (SD). Sample sizes (n), representing independent experiments, are indicated in the figure legends. Statistical analyses were performed using GraphPad Prism 9.5.1. Comparisons across multiple groups were assessed using one-way or two-way analysis of variance (ANOVA), as appropriate. Exact P values are provided in the figures. A P value < 0.05 was considered statistically significant.

Data availability

All datasets generated during this study are available in figshare (https://doi.org/10.6084/m9.figshare.29627516). SAXS data have been deposited in the Small Angle Scattering Biological Data Bank (SASBDB) under accession codes SAS7452 [https://www.sasbdb.org/data/SAS7452/], SAS7469 [https://www.sasbdb.org/data/SAS7469/], SAS7470 [https://www.sasbdb.org/data/SAS7470/] and SAS7473 [https://www.sasbdb.org/data/SAS7473/]. The PDB code of the previously published structure used in this study is 1ED9 [http://doi.org/10.2210/pdb1ED9/pdb]. All data are also available from the corresponding author upon request. Source data are provided as a Source Data file.

Code availability

All custom code central to the conclusions of this study are publicly available at GitHub (https://github.com/iawnix/WatAna). Archived versions of the code are available at Zenodo: CovCom v1.0.0 (https://doi.org/10.5281/zenodo.18617244)[65] and WatAna v1.0.0 (https://doi.org/10.5281/zenodo.18617201)[66].

References

1 Ball, P. Water is an active matrix of life for cell and molecular biology. *Proc. Natl. Acad. Sci. U. S. A.* **114**, 13327-13335 (2017).

2 Chaplin, M. Opinion - do we underestimate the importance of water in cell biology? *Nat. Rev. Mol. Cell Bio.* **7**, 861-866 (2006).

3 Watson, J. L. *et al.* Macromolecular condensation buffers intracellular water potential. *Nature* **623**, 842-852 (2023).

4 Laage, D., Elsaesser, T. & Hynes, J. T. Water dynamics in the hydration shells of biomolecules. *Chem. Rev.* **117**, 10694-10725 (2017).

5 Qin, Y. Z., Wang, L. J. & Zhong, D. P. Dynamics and mechanism of ultrafast water-protein interactions. *Proc. Natl. Acad. Sci. U. S. A.* **113**, 8424-8429 (2016).

6 Israelachvili, J. & Wennerstrom, H. Role of hydration and water structure in biological and colloidal interactions. *Nature* **379**, 219-225 (1996).

7 Fernández, A. & Scheraga, H. A. Insufficiently dehydrated hydrogen bonds as determinants of protein interactions. *Proc. Natl. Acad. Sci. U. S. A.* **100**, 113-118 (2003).

8 Mondal, S., Mukherjee, S. & Bagchi, B. Protein hydration dynamics: Much ado about nothing? *J. Phys. Chem. Lett.* **8**, 4878-4882 (2017).

9 Bellissent-Funel, M. C. *et al.* Water determines the structure and dynamics of proteins. *Chem. Rev.* **116**, 7673-7697 (2016).

10 Ball, P. Water as an active constituent in cell biology. *Chem. Rev.* **108**, 74-108 (2008).

11 Rego, N. B., Ferguson, A. L. & Patel, A. J. Learning the relationship between nanoscale chemical patterning and hydrophobicity. *Proc. Natl. Acad. Sci. U. S. A.* **119**, e2200018119 (2022).

12 Harris, R. C. & Pettitt, B. M. Effects of geometry and chemistry on hydrophobic solvation. *Proc. Natl. Acad. Sci. U. S.A.* **111**, 14681-14686 (2014).

13 Xi, E. T. *et al.* Hydrophobicity of proteins and nanostructured solutes is governed by topographical and chemical context. *Proc. Natl. Acad. Sci. U. S.A.* **114**, 13345-13350 (2017).

14 Chandler, D. Interfaces and the driving force of hydrophobic assembly. *Nature* **437**, 640-647 (2005).

15 Davis, J. G., Gierszal, K. P., Wang, P. & Ben-Amotz, D. Water structural transformation at molecular hydrophobic interfaces. *Nature* **491**, 582-585 (2012).

16 Bandyopadhyay, S., Chakraborty, S. & Bagchi, B. Secondary structure sensitivity of hydrogen bond lifetime dynamics in the protein hydration layer. *J. Am. Chem. Soc.* **127**, 16660-16667 (2005).

17 Nickels, J. D. *et al.* Dynamics of protein and its hydration water: Neutron scattering studies on fully deuterated gfp. *Biophys. J.* **103**, 1566-1575 (2012).

18 Kyte, J. & Doolittle, R. F. A simple method for displaying the hydropathic character of a protein. *J. Mol. Bio.* **157**, 105-132 (1982).

19 Wimberger, L. *et al.* Large, tunable, and reversible ph changes by merocyanine photoacids. *J. Am. Chem. Soc.* **143**, 20758-20768 (2021).

20 Corbella, M., Pinto, G. P. & Kamerlin, S. C. L. Loop dynamics and the evolution of enzyme activity. *Nat. Rev. Chem.* **7**, 536-547 (2023).

21 Zinovjev, K. *et al.* Activation and friction in enzymatic loop opening and closing dynamics. *Nat. Commun.* **15**, 2490 (2024).

22 Stec, B., Holtz, K. M. & Kantrowitz, E. R. A revised mechanism for the alkaline phosphatase reaction involving three metal ions. *J. Mol. Biol.* **299**, 1303-1311 (2000).

23 Chin, J. W. S., S. W.; Martin, A. B.; King, D. S.; Wang, L.; Schultz, P. G. Addition of p-azido-l-phenylalanine to the genetic code of escherichia c oli. *J. Am. Chem. Soc.* **124**, 9026-9027 (2002).

24 Becker, W. *et al.* Fluorescence lifetime imaging by time-correlated single-photon counting. *Microsc. Res. Techniq.* **63**, 58-66 (2004).

25 Bai, Y. L. *et al.* Derivatizing merocyanine dyes to balance their polarity and viscosity sensitivities for protein aggregation detection. *Chem. Commun.* **57**, 13313-13316 (2021).

26 Hou, G. H. & Cui, Q. Stabilization of different types of transition states in a single enzyme active site: QM/MM analysis of enzymes in the alkaline phosphatase superfamily. *J. Am. Chem. Soc.* **135**, 10457-10469 (2013).

27 Mattea, C., Qvist, J. & Halle, B. Dynamics at the protein-water interface from ^{17}O spin relaxation in deeply supercooled solutions. *Biophys. J.* **95**, 2951-2963 (2008).

28 Zheng, C. *et al.* A two-directional vibrational probe reveals different electric field orientations in solution and an enzyme active site. *Nat. Chem.* **14**, 891-897 (2022).

29 Liu, J. F., He, X., Zhang, J. Z. H. & Qi, L. W. Hydrogen-bond structure dynamics in bulk water: Insights from simulations with coupled cluster theory. *Chem. Sci.* **9**, 2065-2073 (2018).

30 Dai, D. H. *et al.* Room-temperature dynamic nuclear polarization enhanced NMR spectroscopy of small biological molecules in water. *Nat. Commun.* **12**, 6880 (2021).

31 Noll, N. & Würthner, F. Bioinspired water preorganization in confined space for efficient water oxidation catalysis in metallosupramolecular ruthenium architectures. *Acc. Chem. Res.* **57**, 1538-1549 (2024).

32 Rego, N. B. & Patel, A. J. Understanding hydrophobic effects: Insights from water density fluctuations. *Annu. Rev. Condens. Matter Phys.* **13**, 303-324 (2022).

33 Gonella, G. *et al.* Water at charged interfaces. *Nat. Rev. Chem.* **5**, 466-485 (2021).

34 Qiao, B. F., Jiménez-Angeles, F., Nguyen, T. D. & de la Cruz, M. O. Water follows polar and nonpolar protein surface domains. *Proc. Natl. Acad. Sci. U. S.A.* **116**, 19274-19281 (2019).

35 Pezzotti, S. *et al.* Terahertz calorimetry spotlights the role of water in biological processes. *Nat. Rev. Chem.* 1-14 (2025).

36 Böhm, F., Schwaab, G. & Havenith, M. Mapping hydration water around alcohol chains by thz calorimetry. *Angew. Chem. Int. Ed.* **56**, 9981-9985 (2017).

37 Pezzotti, S. *et al.* Spectroscopic fingerprints of cavity formation and solute insertion as a measure of hydration entropic loss and enthalpic gain. *Angew. Chem. Int. Ed.* **61**, e202203893 (2022).

38 Lorenz-Fonfria, V. A. Infrared difference spectroscopy of proteins: From bands to bonds. *Chem. Rev.* **120**, 3466-3576 (2020).

39 Rupley, J. A. & Careri, G. Protein hydration and function. *Adv. Protein Chem.* **41**, 37-172 (1991).

40 Woods, D. A. & Bain, C. D. Total internal reflection spectroscopy for studying soft matter. *Soft Matter* **10**, 1071-1096 (2014).

41 Bakulin, A. A., Pshenichnikov, M. S., Bakker, H. J. & Petersen, C. Hydrophobic molecules slow down the hydrogen-bond dynamics of water. *J. Phys. Chem. A* **115**, 1821-1829 (2011).

42 Laage, D. & Hynes, J. T. A molecular jump mechanism of water reorientation. *Science* **311**, 832-835 (2006).

43 Brünig, F. N., Rammler, M., Adams, E. M., Havenith, M. & Netz, R. R. Spectral signatures of excess-proton waiting and transfer-path dynamics in aqueous hydrochloric acid solutions. *Nat. Commun.* **13**, 4210 (2022).

44 Heyden, M. *et al.* Dissecting the THz spectrum of liquid water from first principles via correlations in time and space. *Proc. Natl. Acad. Sci. U. S.A.* **107**, 12068-12073 (2010).

45 Paesani, F., Zhang, W., Case, D. A., Cheatham, T. E., 3rd & Voth, G. A. An accurate and simple quantum model for liquid water. *J. Chem Phys.* **125**, 184507 (2006).

46 Michaud-Agrawal, N., Denning, E. J., Woolf, T. B. & Beckstein, O. Software news and updates mdanalysis: A toolkit for the analysis of molecular dynamics simulations. *J. Comput. Chem.* **32**, 2319-2327 (2011).

47 Du, Z. W. *et al.* The sequence-structure-function relationship of intrinsic erα disorder. *Nature* **638**, 1130-1138 (2025).

48 Lee, Y. *et al.* Ultrafast coherent motion and helix rearrangement of homodimeric hemoglobin visualized with femtosecond x-ray solution scattering. *Nat. Commun.* **12**, 3677 (2021).

49 Gomez, A., Thompson, W. H. & Laage, D. Neural-network-based molecular dynamics simulations reveal that proton transport in water is doubly gated by sequential hydrogen-bond exchange. *Nat. Chem.* **16**, 1838-1844 (2024).

50 Giubertoni, G., Bonn, M. & Woutersen, S. D2o as an imperfect replacement for H2O: Problem or opportunity for protein research. *J. Phys. Chem. B* **127**, 8086-8094 (2023).

51 Grossman, M. *et al.* Correlated structural kinetics and retarded solvent dynamics at the metalloprotease active site. *Nat. Struct. Mol. Biol.* **18**, 1102-U1113 (2011).

52 Li, C., Iscen, A., Palmer, L. C., Schatz, G. C. & Stupp, S. I. Light-driven expansion of spiropyran hydrogels. *J. Am. Chem. Soc.* **142**, 8447-8453 (2020).

53 Kang, E. *et al.* Specific adsorption of histidine-tagged proteins on silica surfaces modified with Ni^{2+}/NTA--derivatized poly(ethylene glycol). *Langmuir* **23**, 6281-6288 (2007).

54 Cha, T., Guo, A. & Zhu, X. Y. Enzymatic activity on a chip: The critical role of protein orientation. *Proteomics* **5**, 416-419 (2005).

55 Maier, J. A. *et al.* Ff14sb: Improving the accuracy of protein side chain and backbone parameters from ff99sb. *J. Chem. Theory Comput.* **11**, 3696-3713 (2015).

56 Frisch, M. J. et al. Gaussian 16, Revision A.03 (Gaussian, Inc., Wallingford, CT, 2016).

57 Wang, J., Wolf, R. M., Caldwell, J. W., Kollman, P. A. & Case, D. A. Development and testing of a general amber force field. *J. Comput. Chem.* **25**, 1157-1174 (2004).

58 Panteva, M. T., Giambasu, G. M. & York, D. M. Comparison of structural, thermodynamic, kinetic and mass transport properties of Mg^{2+} ion models commonly used in biomolecular simulations. *J. Comput. Chem.* **36**, 970-982 (2015).

59 Li, P. F. & Merz, K. M. Taking into account the ion-induced dipole interaction in the nonbonded model of ions. *J. Chem. Theory Comput.* **10**, 289-297 (2014).

60 Case, D. A. et al. AMBER 23 (University of California, San Francisco, 2023).

61 Cock, P. J. A. *et al.* Biopython: Freely available python tools for computational molecular biology and bioinformatics. *Bioinformatics* **25**, 1422-1423 (2009).

62 Rdkit/rdkit: 2024_09_5 (q3 2024) release (release_2024_09_5) v. 2024_09_5 (Zenodo, 2025).

63 Tosco, P., Stiefl, N. & Landrum, G. Bringing the MMFF force field to the RDKit: implementation and validation. *J. Cheminform.* 6, 37 (2014).

64 Wilson, P. H. B. S. R. W. K. R. Molecular dynamics and spectra. II. Diatomic raman. *J. Chem. Phys.* **75**, 515-529 (1981).

65 iawnix. iawnix/CovCom: v1.0.0 (v1.0.0). Zenodo. https://doi.org/10.5281/zenodo.18617244 (2026).

66 iawnix. iawnix/WatAna: v1.0.0 (v1.0.0). Zenodo. https://doi.org/10.5281/zenodo.18617201 (2026).

Acknowledgment

This work was supported by the National Key R&D Program of China (2024YFA1700050, 2019YFA0905200), the National Natural Science Foundation of China (22225403, 22204053, 92477103, 22273023), Shanghai Municipal Science and Technology Commission with Grant (25511102400), Shanghai Municipal Natural Science Foundation (23ZR1418200), Natural Science Foundation of Chongqing, China (CSTB2023NSCQ-MSX0616), Shanghai Frontiers Science Center of Molecule Intelligent Syntheses, Shanghai Future Discipline Program (Quantum Science and Technology), Shanghai Municipal Education Commission's "Artificial Intelligence-Driven Research Paradigm Reform and Discipline Advancement Program", and the Fundamental Research Funds for the Central Universities. East China Normal University "Artificial Intelligence" Seed Grant Program (40500-20101-222438). We acknowledge the Shanghai Synchrotron Radiation Facility (SSRF) BL06B beamline (https://cstr.cn/31124.02.SSRF.BL06B) for experimental measurement assistance, and the BL19U2 beamline (https://cstr.cn/31129.02.NFPS.BL19U2) at the National Facility for Protein Science in Shanghai (NFPS, https://cstr.cn/31129.02.NFPS) for technical support with data collection and analysis. We also thank the Supercomputer Center of East China Normal University (ECNU Multifunctional Platform for Innovation 001) for providing computer resources.

Author contributions

Y.Y.L. and D.L. conceived the study and designed experiments. J.H.Z. and X.H. performed and analyzed molecular dynamics simulations. Y.Y.L. conducted THz spectroscopy, SAXS measurements, and enzymatic activity assays. J.J.G. and H.Y.G. carried out fluorescence lifetime experiments and analyzed the corresponding data. S.S.C. and D.M. engineered, expressed, and purified mutant ALP variants. H.W.Z. optimized data visualization. B.S. guided the analytical for THz data interpretation. Y.Y.L. and D.L. prepared the manuscript draft and created key figures, with critical revisions from all authors. D.L., D.M., and X.H. supervised the project. Y.Y.L. and J.H.Z. contributed equally to this work.

Competing interests

The authors declare no competing interests.

Fig. 1 Light-induced regulation of the hydrophobicity changes of a specific residue on Alkaline Phosphatase (ALP). (a) Reversible photoisomerization between merocyanine (MC) and spiropyran (SP) accompanied by a large shift in molecular dipole moment (μ) (in Debye). (b) Light-regulated wettability changes of SP-coated glass surface. (c) Schematic illustration of the site-specific engineering of ALP with SP. p-azido-L-phenylalanine (pAzF) mutagenesis was introduced at E406 and E906 sites of loop regions. DBCO-conjugated spiropyran (DBCO-SP) was then conjugated to the engineered ALP via click reaction. (d) Deconvoluted LC-MS mass spectra of ALP-mutation and ALP-SP conjugate. (e) UV/vis spectra of ALP-SP and ALP-MC under different light stimuli. (f) TCSPC decay curves of ALP-MC and ALP-RMC, generated by single-molecule experiments. Insets: fluorescence lifetime images of ALP-MC and ALP-RMC molecules in the single-molecule experiment. Scale bar: 2 μm. (g) Comparison of lifetime changes between MC and RMC states for both conjugated (ALP-modified) and free MC molecules. Data are represented as mean ± SD from six independent experiments (n = 6). Statistical significance was determined by two-way ANOVA followed by Šídák's multiple comparisons test. ns, not significant ($p > 0.05$). Points indicate individual samples.

Fig. 2 MD simulations of the site-specific photoisomerization-induced hydration dynamic changes. (a-c) Radial distribution functions between waters and the modified residue (a), catalytic site (b), or the overall ALP surface (c) for both ALP-MC and ALP-SP. Inserts are the enlarged differences between ALP-MC and ALP-SP. (d) Schematic illustration of competitive hydrogen bonding between hydrophilic MC and water. (e-g) Comparison of HB lifetimes between water-water (w-w) ($\tau_{HB,\,w\text{-}w}$) within distinct hydration shells between ALP-MC and ALP-SP for modified site (e), catalytic site (f), and global ALP (g). Data shown in (a-c, e-g) are presented as mean ± SD from four independent MD simulations (n = 4), each initiated from the same equilibrated structure with randomized initial velocities. Statistical significance in (e-g) was determined by two-way ANOVA followed by Šídák's multiple comparisons test. ns, not significant. (h) Schematic diagram of local water disturbance propagation pathway. (i) Probability distribution of the group-specific water density fluctuations ($[\langle N^2\rangle-\langle N\rangle^2]/\langle N\rangle$), calculated within spherical volumes around each surface residue group of ALP-MC and ALP-SP. (j) The differences in hydro-patches in the number of H-bonded water molecules ($\Delta N_{\text{H-bonded water}}$) per residue between ALP-MC and ALP-SP (calculated as ALP-SP – ALP-MC). Red patches indicate an increased value of $N_{\text{H-bonded water}}$, while blue patches indicate a decrease. (k-n) The difference value in H-bonded waters ($\Delta N_{\text{H-bonded water}}$) (top) and the corresponding frequency of $\Delta N_{\text{H-bonded water}}$ (bottom) are shown for negatively charged residues (k), positively charged residues (l), polar (neutral) residues (m), and nonpolar residues (n) of ALP-MC and ALP-SP.

Fig. 3 ATR-THz spectroscopy probes the hydration dynamic changes between ALP-MC and ALP-SP. (a) Schematic illustrating the heterogeneous hydration interface of a protein, with bound water around hydrophilic patches and wrapped water around hydrophobic patches. (b-c) Water coverage at protein interfaces under moderate hydration (~ 0.7 g/g; b) and low hydration (~ 0.2 g/g; c) conditions. (d) ATR-THz absorption spectra for ALP-MC and ALP-SP at hydration levels spanning low (~ 0.2 g/g) to high (~ 1.2 g/g). Hydration levels are given in g/g (g H_2O per g protein). (e-f) Hydration-dependent frequency shifts in THz absorption peaks for the wrap-water region (150-200 cm^{-1}) (f) and the bound-water region (450-600 cm^{-1}). (g) The difference absorption coefficient ($\Delta\alpha(\nu)$) spectra in ALP-MC and ALP-SP systems. The black arrow denotes the slope of $\Delta\alpha/\Delta\nu$, obtained from fitting spectra between 500 and 600 cm^{-1} with varying hydration levels. The data shown in (e-g) are presented as mean ± SD from three independent experiments (n = 3). (h) MD-calculated THz spectra of the first hydration layer surrounding the MC/SP-modified sites.Inset: schematic illustration of the hydrated modified site. (i) MD-calculated THz spectra of the global hydration layer for both ALP-MC and ALP-SP, excluding regions modified by MC/SP. Inset: schematic illustration of the hydrated protein with the modified site excluded. The data in (h, i) are presented as mean ± SD from four independent MD simulations (n = 4).

Fig. 4 Global structural changes of ALP induced by photoisomerization at the individual residue. (a) Backbone RMSD evolution during MD simulation relative to the initial structure. The data are presented as the mean ± SD from four independent MD simulations (n = 4). (b) ΔRMSF of protein backbone atoms (C, C_α, N, O) between ALP-MC and ALP-SP as a function of residue sequence number. (c) ΔRMSF values on corresponding residues across the ALP structure. Color bar: averaged ΔRMSF values (in Angstroms). (d) The superimposed MD-simulated structures of ALP-MC and ALP-SP, and the enlarged view of the regions containing modified-SP and the catalytic active site. (e,f) Averaged distance matrices illustrating intrapeptide contacts between residues for the ALP-MC (e) and ALP-SP (f). Color bar: average intra-residue distances (in Angstroms). (g) Final SAXS scattering profiles (plotted as logI(q) *vs* q, where $q = 4\pi\sin\theta/\lambda$) of ALP-MC and ALP-SP. (h) The linear region of the Guinier plot for ALP-MC and ALP-SP, from which Rg and I(0) can be derived. (i) Distance probability functions, p(r) of the two samples. (j) Scattering curve of the two samples shown in dimensionless Kratky plots ($(qRg)^2I(q)/I(0)$ vs. qRg). The data shown in (g-j) are presented as the mean ± SD from three independent experiments.

Fig. 5 Enzymatic catalytic changes of ALP induced by photoisomerization at the individual residue. (a) Hydrophilic substrate, pNPP, and hydrophobic substrates, 4-MUP, to interrogate the hydration-regulated enzymatic activity. (b) Michaelis-Menten kinetics for the hydrolysis of pNPP by ALP-MC and ALP-SP, respectively; Inset: the derived K_m and k_{cat} values. (c) Solvent isotope effects on light-induced enzymatic changes in H_2O/D_2O buffers using pNPP as a substrate. (d) Michaelis-Menten kinetics for the hydrolysis of 4-MUP; Inset: the derived K_m and k_{cat} values. (e) Solvent isotope effects on light-induced enzymatic changes in H_2O/D_2O buffers using 4-MUP as a substrate. The data in (b, d) are presented as the mean ± SD from three independent experiments (n = 3). Data in (c,e) are presented as mean ± SD from four independent experiments (n = 4). Statistical significance in (c,e) was assessed by two-way ANOVA followed by Šídák's multiple comparisons test. ns, not significant.

Editorial Summary

By engineering single residue of protein with a light-switchable molecule, this study reveals that local hydrophobicity propagates through hydrogen bond network to reshape protein structure and function, shifting the paradigm to structure–hydration– function.

Peer review information: *Nature Communications* thanks the anonymous reviewers for their contribution to the peer review of this work. A peer review file is available.

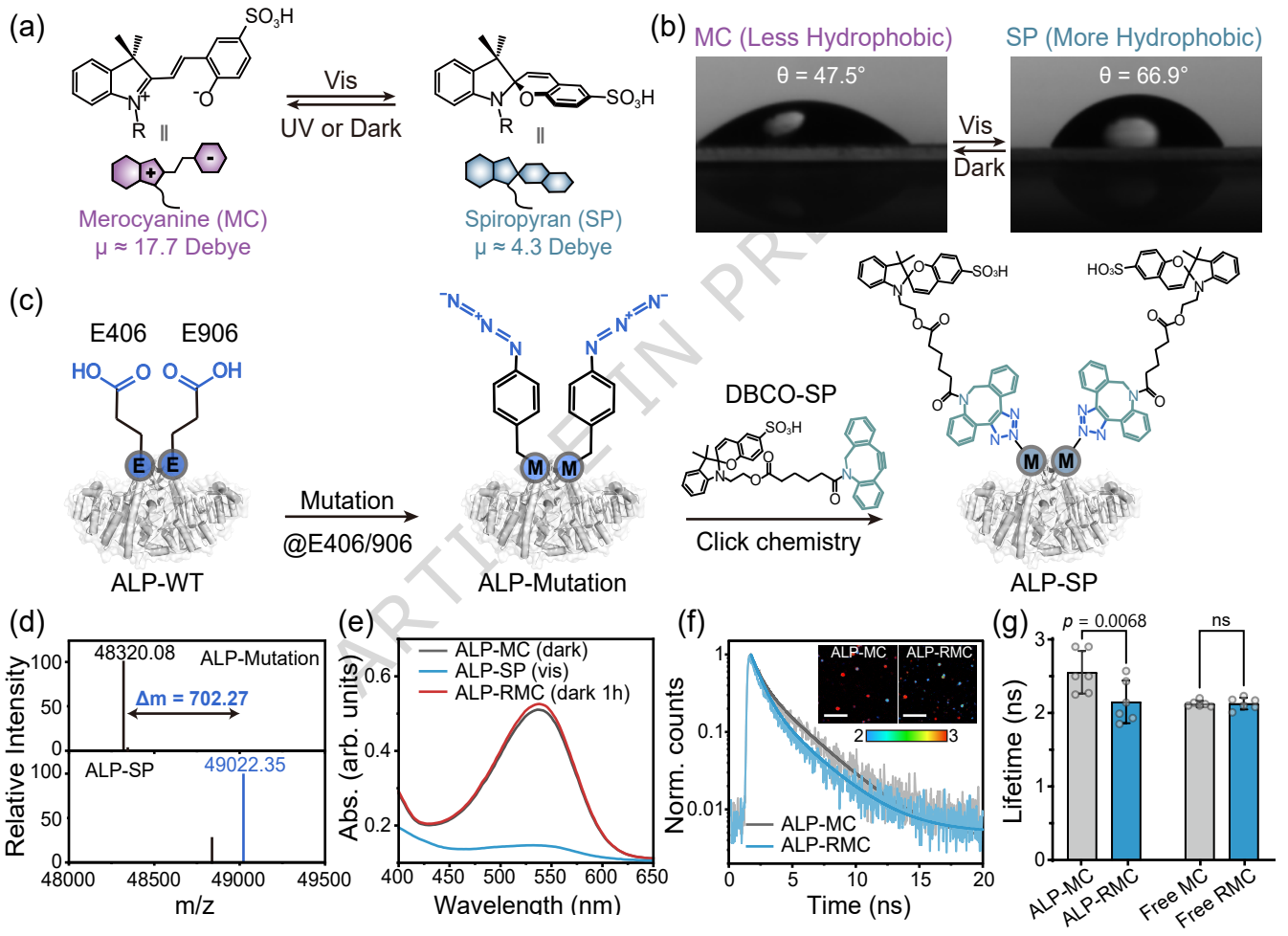
(a)
SO3H
Vis
UV or Dark
Merocyanine (MC)
μ ≈ 17.7 Debye
Spiropyran (SP)
μ ≈ 4.3 Debye
(b)
MC (Less Hydrophobic)
SP (More Hydrophobic)
θ = 47.5°
θ = 66.9°
Vis
Dark
(c)
E406
E906
ALP-WT
Mutation
@E406/906
ALP-Mutation
DBCO-SP
Click chemistry
ALP-SP
(d)
48320.08
ALP-Mutation
Δm = 702.27
ALP-SP
49022.35
Relative Intensity
m/z
(e)
ALP-MC (dark)
ALP-SP (vis)
ALP-RMC (dark 1h)
Abs. (arb. units)
Wavelength (nm)
(f)
ALP-MC
ALP-RMC
Norm. counts
Time (ns)
(g)
p = 0.0068
ns
Lifetime (ns)
ALP-MC
ALP-RMC
Free MC
Free RMC

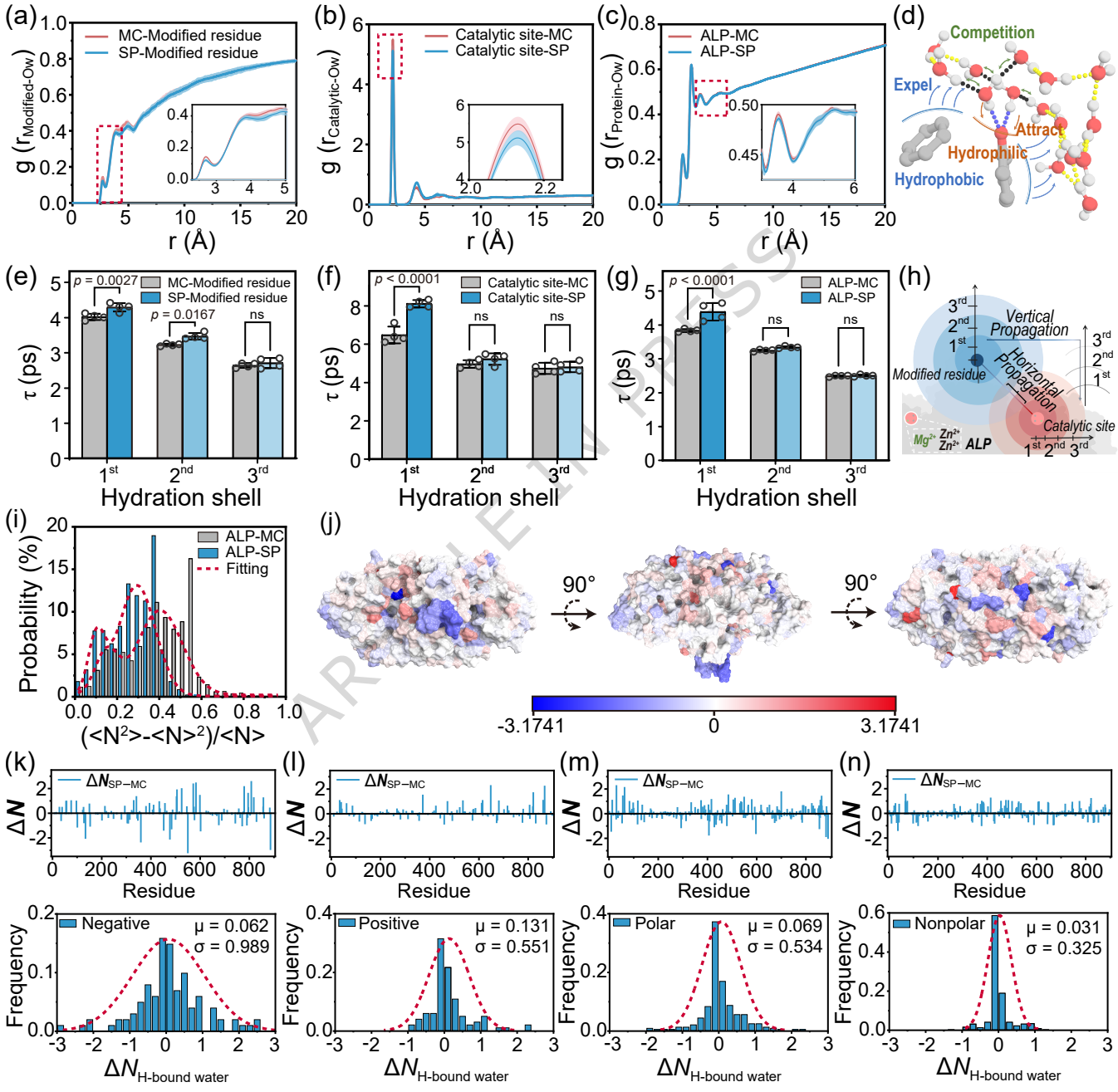
(a)
MC-Modified residue
SP-Modified residue
g (r Modified-Ow)
r (Å)
(b)
Catalytic site-MC
Catalytic site-SP
g (r Catalytic-Ow)
r (Å)
(c)
ALP-MC
ALP-SP
g (r Protein-Ow)
r (Å)
(d)
Competition
Expel
Attract
Hydrophilic
Hydrophobic
(e)
p = 0.0027
p = 0.0167
ns
MC-Modified residue
SP-Modified residue
τ (ps)
Hydration shell
(f)
p < 0.0001
Catalytic site-MC
Catalytic site-SP
ns
τ (ps)
Hydration shell
(g)
p < 0.0001
ALP-MC
ALP-SP
ns
τ (ps)
Hydration shell
(h)
Vertical Propagation
Horizontal Propagation
Modified residue
Catalytic site
ALP
(i)
ALP-MC
ALP-SP
Fitting
Probability (%)
(<N²>-<N>²)/<N>
(j)
90°
90°
-3.1741
0
3.1741
(k)
ΔN SP−MC
ΔN
Residue
Negative
μ = 0.062
σ = 0.989
Frequency
ΔN H-bound water
(l)
ΔN SP−MC
ΔN
Residue
Positive
μ = 0.131
σ = 0.551
Frequency
ΔN H-bound water
(m)
ΔN SP−MC
ΔN
Residue
Polar
μ = 0.069
σ = 0.534
Frequency
ΔN H-bound water
(n)
ΔN SP−MC
ΔN
Residue
Nonpolar
μ = 0.031
σ = 0.325
Frequency
ΔN H-bound water

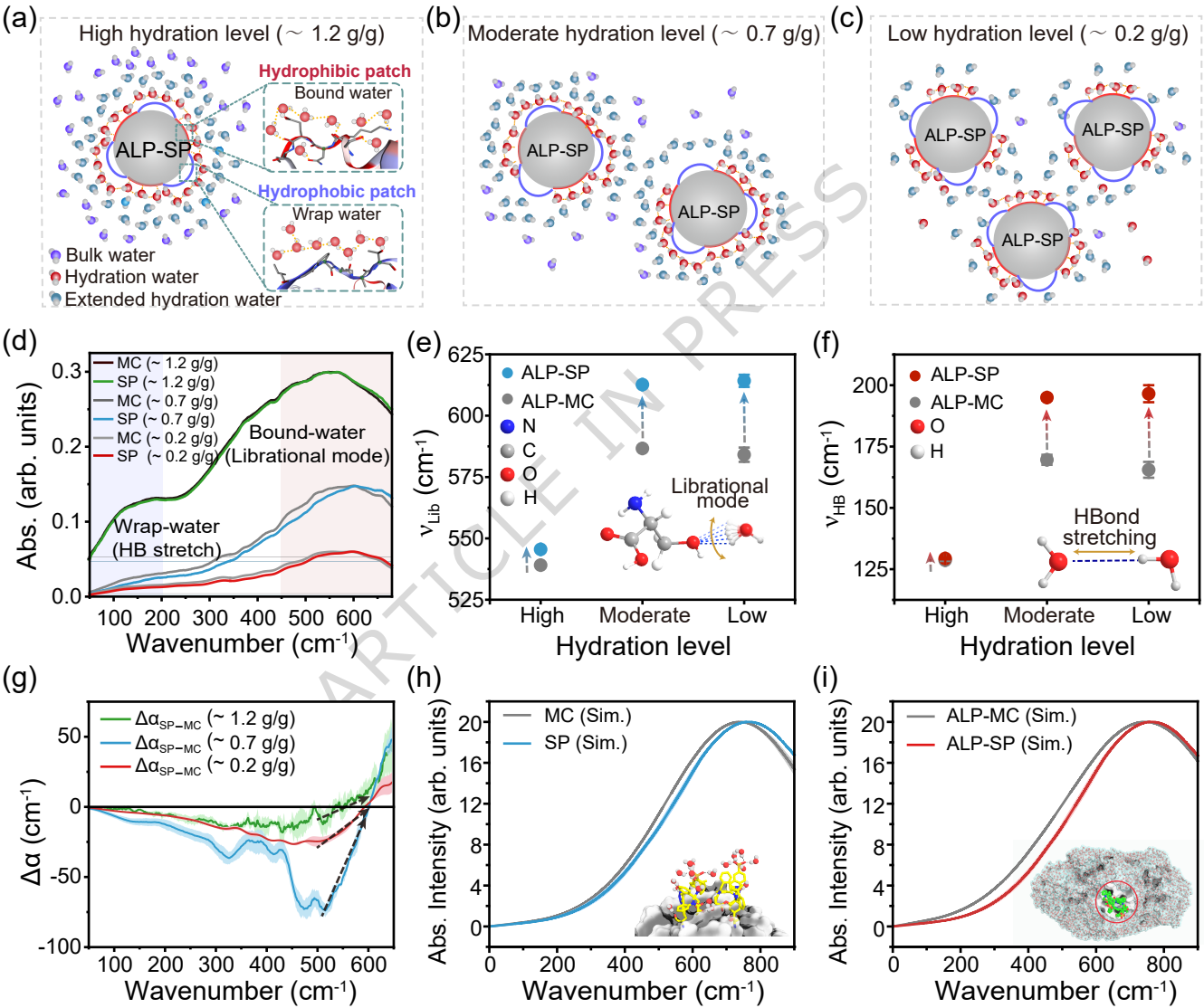
(a)
High hydration level (~ 1.2 g/g)
ALP-SP
Hydrophibic patch
Bound water
Hydrophobic patch
Wrap water
Bulk water
Hydration water
Extended hydration water
(b)
Moderate hydration level (~ 0.7 g/g)
ALP-SP
ALP-SP
(c)
Low hydration level (~ 0.2 g/g)
ALP-SP
ALP-SP
ALP-SP
(d)
MC (~ 1.2 g/g)
SP (~ 1.2 g/g)
MC (~ 0.7 g/g)
SP (~ 0.7 g/g)
MC (~ 0.2 g/g)
SP (~ 0.2 g/g)
Bound-water (Librational mode)
Wrap-water (HB stretch)
Abs. (arb. units)
Wavenumber (cm-1)
(e)
ALP-SP
ALP-MC
N
C
O
H
Librational mode
νLib (cm-1)
High
Moderate
Low
Hydration level
(f)
ALP-SP
ALP-MC
O
H
HBond stretching
νHB (cm-1)
High
Moderate
Low
Hydration level
(g)
Δαsp−mc (~ 1.2 g/g)
Δαsp−mc (~ 0.7 g/g)
Δαsp−mc (~ 0.2 g/g)
Δα (cm-1)
Wavenumber (cm-1)
(h)
MC (Sim.)
SP (Sim.)
Abs. Intensity (arb. units)
Wavenumber (cm-1)
(i)
ALP-MC (Sim.)
ALP-SP (Sim.)
Abs. Intensity (arb. units)
Wavenumber (cm-1)